

See discussions, stats, and author profiles for this publication at: <https://www.researchgate.net/publication/276293979>

Facile Synthesis of Rod–Coil Block Copolymers with Chiral, Helical Polycarbodiimide Segments via Postpolymerization CuAAC " Click " Coupling of Functional End Groups

ARTICLE *in* MACROMOLECULES · MAY 2015

Impact Factor: 5.8 · DOI: 10.1021/acs.macromol.5b00453

CITATIONS

2

READS

43

6 AUTHORS, INCLUDING:



James F Reuther

University of Texas at Austin

9 PUBLICATIONS 50 CITATIONS

[SEE PROFILE](#)



Dumindika Siriwardane

University of Texas at Dallas

9 PUBLICATIONS 10 CITATIONS

[SEE PROFILE](#)



Raymond Campos

University of Texas at Dallas

11 PUBLICATIONS 84 CITATIONS

[SEE PROFILE](#)



Bruce Novak

University of Texas at Dallas

135 PUBLICATIONS 5,654 CITATIONS

[SEE PROFILE](#)

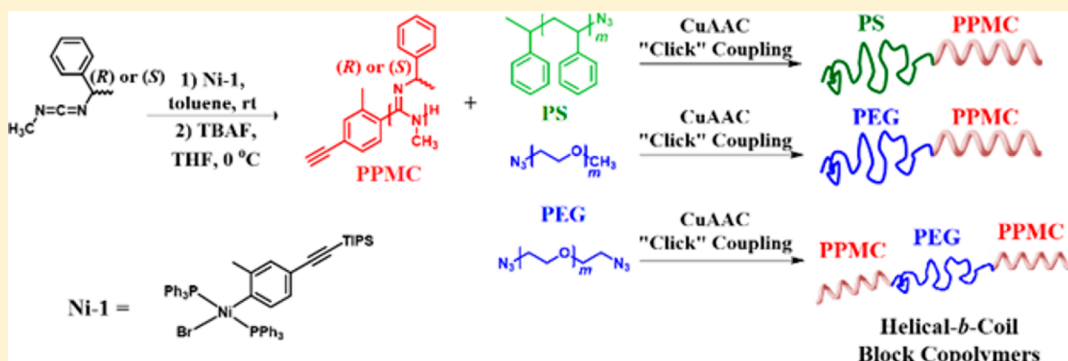
Facile Synthesis of Rod–Coil Block Copolymers with Chiral, Helical Polycarbodiimide Segments via Postpolymerization CuAAC “Click” Coupling of Functional End Groups

James F. Reuther,^{†,‡} Dumindika A. Siriwardane,[†] Oleg V. Kulikov,[†] Benjamin L. Batchelor,[†] Raymond Campos,[†] and Bruce M. Novak*,[†]

[†]Department of Chemistry and Alan G. MacDiarmid NanoTech Institute, University of Texas at Dallas, Richardson, Texas 75080, United States

[‡]Department of Chemistry, University of Texas at Austin, Austin, Texas 78712, United States

Supporting Information



ABSTRACT: Using the living nickel(II)-mediated polymerization of carbodiimides, the chiral (*R*)- or (*S*)-*N*-1-phenethyl-*N'*-methylcarbodiimide (PMC) monomers were polymerized with a new TIPS protected alkyne functional nickel initiator forming PPMC with an excess single-handed screw sense and the alkyne moiety covalently attached to the terminus of the polymer, as confirmed by ¹H NMR and MALDI-TOF MS. After deprotection, the alkyne end groups of rigid-rod PPMC-2 were coupled with azide-terminated, random-coil PS and PEG homopolymers forming a novel class of helical-*b*-coil block copolymers. In the thin-film, all synthesized diblock copolymers formed interesting nanofibular morphologies when subject to specific conditions. The triblock RCP-4, however, adopted unique macroporous morphology as identified by AFM and SEM with average pore diameters of ca. 832 ± 194 nm. The origin of this was found to be associated with the ordering of large, hollow vesicle aggregates upon solvent evaporation followed by the melting of these aggregates filling in the hollow interior forming the submicron pores observed. Furthermore, the size of these aggregates can be easily modulated in a linear fashion from 272 to 1648 nm simply by increasing the concentration of RCP-4 in THF. Finally, the three PPMC-PEG copolymers synthesized were found to adopt lyotropic cholesteric mesophases in concentrated toluene solutions (ca. 30 wt %).

INTRODUCTION

The tunable self-assembly and microphase separation of conventional coil–coil block copolymer (CCP) have been studied and modeled extensively.^{1,2} The ability to covalently bind polymers of varying composition and structure allows for the combination of polymer properties often with synergistic effects and expanded function. The self-assembly of these macromolecules is governed by a variety of noncovalent forces such as hydrophobic/hydrophilic interactions, electrostatic interactions, hydrogen bonding, and microphase separation. To date, directed block copolymer self-assembly remains as one of the most powerful, versatile methods of tailoring nanometer-size features.

The synthesis of rigid rod-*b*-random coil block copolymers, however, has only recently attracted significant attention due to their unique capabilities to form stable supramolecular structures

with a wide array of unique self-assembly behaviors observed in solution and the solid state.^{3–6} The anisotropic nature of rigid-rod blocks characteristically results in lyotropic/thermotropic liquid crystallinity with nematic or highly ordered smectic mesophases adopted in solution and/or in the melt.^{7,8} Therefore, the assembly behaviors of rod–coil block copolymers (RCP) in solution and the solid state vastly differ from those of CCPs arising from a combination of microphase immiscibility of the two blocks and the self-organization behaviors of the rigid-rod block.

Received: March 3, 2015

Revised: April 27, 2015

The rodlike blocks typically consist of polymeric/oligomeric π -conjugated and/or helical segments offering significant potential in applications such as organic electronics, biological mimics, drug delivery, and high performance composites. A variety of structurally diverse π -conjugated systems have been incorporated into RCPs including oligophenylenes,⁹ oligo(*p*-vinylenephylene),¹⁰ oligo(*p*-benzamide),^{11,12} polyfluorenes,^{13,14} polythiophenes,^{15,16} and poly(phenylquinolone).^{17–19}

Additionally, naturally occurring and synthetic helical macromolecules have been coupled with conventional random-coil polymers. Polypeptides are, by far, the most common helical, rigid-rod block incorporated into RCPs including such systems as poly(*γ*-benzyl-L-glutamate),^{7,20–23} poly(L-lysine),^{24,25} and poly(L-glutamic acid).²⁶ Loos et al. reported the synthesis and self-assembly of a series of block copolymers with chiral, naturally occurring amylose polysaccharide blocks and synthetic, random-coil polystyrene (PS) blocks.²⁷ Fully synthetic helical macromolecules have been slow to make the transition into RCPs with the exception of poly(*n*-hexyl isocyanate) (PHIC), which has been combined with conventional polymer systems such as PS²⁸ and poly(ethylene glycol) (PEG).^{29–31}

Furthermore, Satoh et al. synthesized functional Ti(IV) initiators to incorporate alkyne and azide moieties onto the PHIC terminus for subsequent copper-catalyzed alkyne–azide cycloaddition (CuAAC) “click” coupling.³² This was accomplished by appending these specific functionalities to the alkoxide ligand bound to the Ti(IV) center which transfers to the first isocyanate monomer unit upon initiation. These end-functionalized PHIC homopolymers were then coupled with various polymer systems forming a novel class of RCPs. This proved to be an efficient method but only PHIC homopolymers with molecular weights (MW) of ~ 12 kDa were successfully isolated. Additionally, the air and moisture sensitivity of these Ti(IV) initiators provides substantial difficulties in the synthesis, purification, and application of these complexes.

Similar Ti(IV) systems have also been shown to readily polymerize carbodiimides in the same living fashion as isocyanates (Scheme 1).³³ These polycarbodiimides adopt a

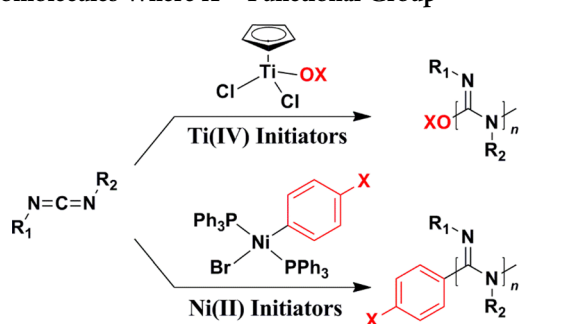
η^1 -aryl ligand acts as the necessary initiator ligand transferring from the Ni(II) metal center to the electrophilic center carbon of the carbodiimide monomer. Upon work-up, the aryl ligand remains covalently attached to the terminus of the polymer chain as confirmed by ¹H NMR and MALDI-TOF MS.

The enhanced stability of these Ni(II) complexes allows for the much simpler synthesis and purification procedures when compared with their Ti(IV) counterparts. This, in turn, allows for the facile formation of functional Ni(II) initiators with latent reactive groups appended to the 4-position of the η^1 -aryl ligand. Upon polymerization, these functionalities will be appended to the terminus of the polycarbodiimide and can be utilized postpolymerization. Herein, we report the synthesis and utilization of the triisopropylsilyl (TIPS) protected alkyne functional Ni(II) initiator (Ni-1) to specifically end-functionalize chiral, helical poly(*N*-1-phenethyl-*N'*-methylcarbodiimide) (PPMC). When incorporating enantiopure side chains, PPMC has been shown to adopt a rigid-rod conformation in solution with experimentally determined persistence lengths (*P*) of ca. 42 \pm 8 nm.⁴¹ Additionally, this polymer adopts lyotropic cholesteric mesophases in concentrated CHCl₃ solutions.³⁵

The use of CuAAC “click” reactions in macromolecular synthesis has expanded tremendously offering new routes in the synthesis of rod–coil block copolymers, core–shell nanoparticles, and rod–coil polymer brushes.^{42–45} Our group has successfully demonstrated the ability to efficiently functionalize the side chains of polycarbodiimides using CuAAC “click” chemistry in several reports.^{46–48} Taking advantage of postpolymerization CuAAC click reactions between alkyne-terminated PPMC and azide-terminated PEG/PS, a series of helical-*b*-random coil RCPs were synthesized. The thermal properties of these copolymers were characterized by DSC and TGA showing distinct thermal characteristics corresponding to both blocks. Additionally, the thin-film morphologies and aggregation behaviors of these copolymers were studied by tapping-mode atomic force microscopy (AFM), scanning electron microscopy (SEM), polarizing optical microscopy (POM), and dynamic light scattering (DLS).

RESULTS AND DISCUSSION

End-Functionalization of PPMC. The Ni(II) initiators reported previously displayed substantially improved air and moisture stability in the solid state when compared with their Ti(IV) counterparts. In solution and in the absence of monomer, however, these complexes quickly decompose in ca. 30 min via disproportionation. Appending the *o*-methyl substituent to the aryl ligand drastically enhances the solution stability according to previous reports.⁴⁹ For this reason, we incorporated the same methyl substituent in the synthesis of Ni-1. The corresponding TIPS-alkyne functionalized aryl bromide was synthesized via Sonogashira cross-coupling and then reacted with bis(1,5-cyclooctadiene)nickel(0) (Ni(COD)₂) in the presence of triphenylphosphine forming the trans-substituted nickel(II) complex Ni-1 (Scheme 2). The added solution stability (ca. >24 h) of Ni-1 allows for full characterization by ¹³C NMR, ¹H NMR, and ³¹P NMR. The appearance of the single peak at 21.0 ppm in the ³¹P NMR of this initiator confirms the formation of the desired trans-substituted nickel(II) complex and is comparable to previously reported chemical shifts of similar complexes (Figure S1).^{40,49} The ¹H NMR, ¹³C NMR, and HRMS-ESI characterization data for Ni-1 can also be found in the Supporting Information.



rigid-rod, helical conformation stemming from the partial conjugation of the guanidine-like backbone and steric repulsion of adjacent pendant groups, respectively. These interesting materials possess a blend of fruitful properties including liquid crystallinity,^{34,35} chiral sensing,³⁶ and chiroptical switching.^{37–39} Recently, we reported the new living polymerization of carbodiimides initiated and mediated by air and moisture stable bis(triphenylphosphino)aryl nickel(II) bromide complexes.⁴⁰ In a similar manner to the alkoxide ligand on Ti(IV) initiators, the

Scheme 2. Synthesis of Protected Alkyne-Functionalized Ni-1 via Oxidative Addition of the Corresponding Aryl Bromide with $\text{Ni}(\text{COD})_2$ and Its Application in the Polymerization of PMC Forming the Protected Alkyne-Terminated PPMC-1; Deprotection of the TIPS Group with TBAF Affords the Deprotected PPMC-2

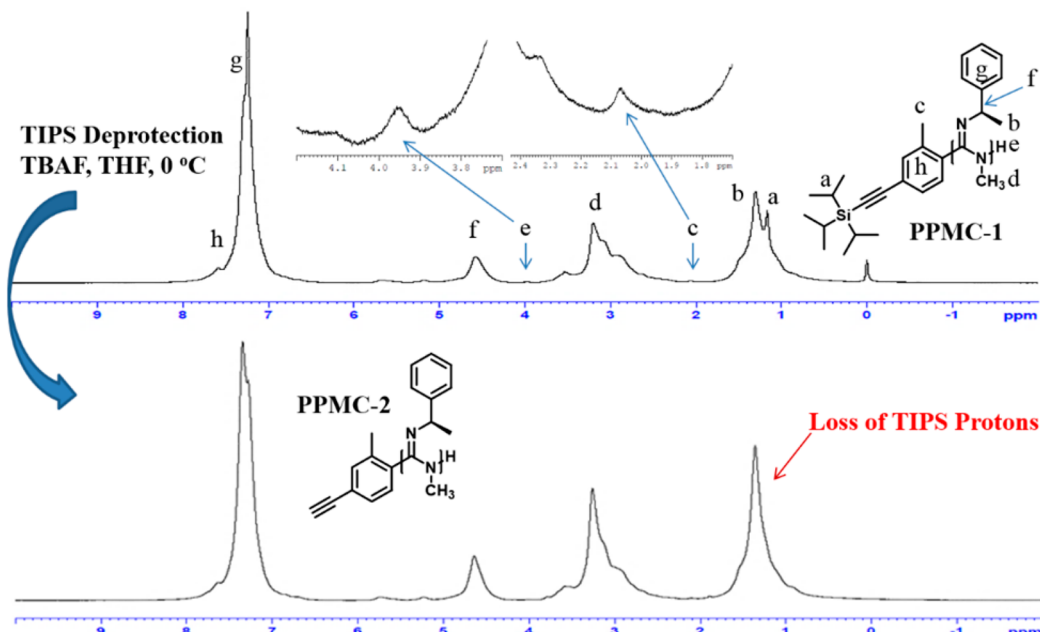
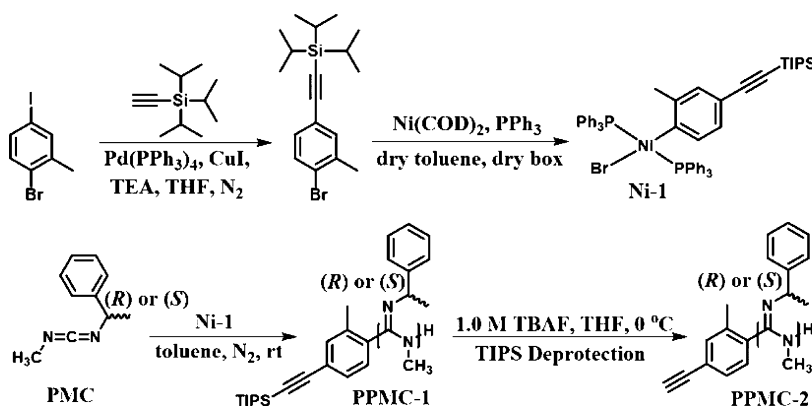


Figure 1. ^1H NMR spectra of PPMC-1 and -2 showing clear chemical shifts associated with the functional end groups and clear disappearance of the chemical shift associated with the TIPS group upon deprotection.

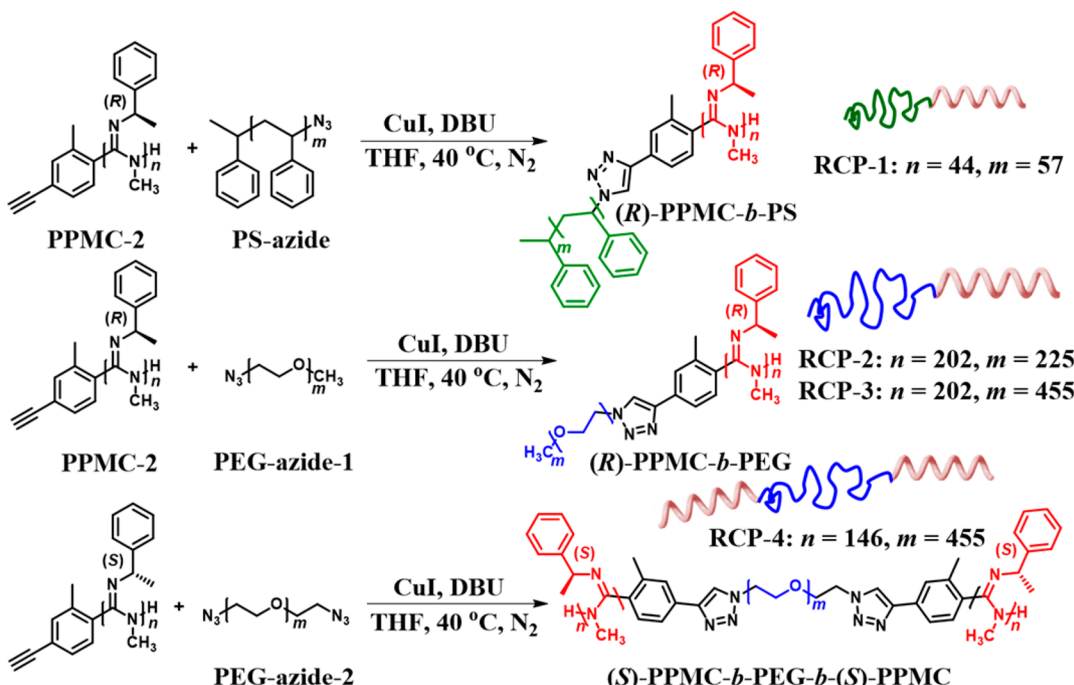
This complex was applied in the polymerization of the chiral PMC monomer forming the rigid-rod, mesogenic polycarbodiimide PPMC-1 with the protected alkyne functional end group (Scheme 2). The resulting polymerization is very fast and efficient providing near-quantitative yields (ca. 92–96%) within ~90 min, giving this initiator comparable activity to the previously reported Ni(II) initiators. The ^1H NMR of PPMC-1 clearly shows specific chemical shifts attributed to the aryl end group with peaks at ca. 1.09 and 2.05 ppm, corresponding to the TIPS protons and the *o*-methyl substituent, respectively (Figure 1). Additionally, the aryl protons are slightly visible at 7.52 ppm, although overlapped with the pendant aryl protons. The *o*-methyl group provides a handle for determining molecular weight by end group analysis using its relative integration with respect to the pendant methine proton at 4.62 ppm.

The opposite terminus of the polymer was previously shown to become protonated upon precipitation in MeOH during work-up as evident of MALDI-TOF MS.⁴⁰ The proton associated with this end group is also visible at 3.96 ppm in the

^1H NMR of PPMC-1. To confirm this, the polymer was redissolved in $\text{THF}-d_8$, and ~2 drops of D_2O were added to the NMR sample, causing the peak to disappear in the spectra. This suggests that these protons are exchangeable, providing further evidence that these peaks correlate with the terminal N-H. Additionally, ^{13}C NMR spectroscopy was conducted on PPMC-1 providing additional evidence for the intact functionality appended to the end group (Figure S4).

The deprotection of the TIPS protecting group with tetrabutylammonium fluoride (TBAF) can also be monitored by ^1H NMR with the complete disappearance of the TIPS chemical shift after ~2 h reacting at 0 °C. The ^1H NMR spectrum of the deprotected alkyne-terminated PPMC-2 can also be found in Figure 2, showing no other changes in the characteristic pendant and end group chemical shifts. The terminal alkyne proton could not be observed in the ^1H NMR spectra following deprotection most likely due to overlap pendant group methyl chemical shifts. However, the ^{13}C chemical shifts associated with the TIPS protecting group at 11.5 and 18.8 ppm completely

Scheme 3. CuAAC “Click” Coupling of PPMC-2 with Azide-Terminated PS and PEG Forming a New Class of Helical-*b*-Random Coil RCPs



disappear following TBAF deprotection, and a new chemical shift forms at 31.2 ppm corresponding to the terminal, deprotected alkyne carbon (Figure S6).

To accurately confirm the presence of the intact functionality appended to the terminus of the polymer, MALDI-TOF MS was applied to quantitatively measure the masses of specific polymer chains of different MWs. Similar to previously reported examples, only low-MW polymer chains ablate and reach the detector with an upper threshold of ~4500 Da for PPMC-1 (Figure S5). The theoretical *m/z* values of PPMC with 11–15 repeat units (ca. 160.10 Da) were calculated with the protected alkyne functional aryl group (ca. 271.19 Da) and hydrogen (ca. 1.01 Da) as the two termini. In addition, the ionization source necessary for detection was found to be protonation of the basic polymer backbone, similar to previous examples. The observed mass distribution in the experimental MALDI-TOF MS matches closely (± 1.0 Da) with the calculated *m/z* values. The corresponding mass loss to the removal of the TIPS protecting group (ca. 156.24 Da) was also observed in the MALDI-TOF MS of PPMC-2, confirming the full deprotection of the TIPS protecting group within 2 h of reacting (Figure S7).

Rod–Coil Block Copolymer Formation via CuAAC “Click” Reaction. Using postpolymerization modifications of the functional alkyne end groups in PPMC-2, a series of RCPs were synthesized via CuAAC “click” reaction of the alkyne moiety with azide-terminated PS and PEG (Scheme 3).

The conversion of this reaction can be monitored by the disappearance of the azide stretching mode at 2107 cm^{-1} in the FTIR spectrum. Accurately controlling the stoichiometry of the two polymers proved to be challenging due to difficulties in determining the MW of polycarbodiimides using GPC.³³ Polycarbodiimides typically display significant adhesion to the polystyrene stationary phase in GPC resulting in skewed MW and inflated dispersity index (D) values atypical of living polymerizations. Adding small amounts (~0.5 vol %) of specific additives, in this case 1,8-diazabicycloundec-7-ene (DBU), to the

GPC solvent mobile phase has been shown to decrease the affinity of polycarbodiimides, but some trailing is still observed causing the slightly larger than expected D values reported herein.⁴⁰ ^1H NMR integration of the *o*-methyl substituent on the end group relative to the methine hydrogen on the pendant group provided accurate estimations of M_n for subsequent “click” postpolymerization modifications when coupled with GPC. Unfortunately, neither the terminal alkyne proton nor the resulting triazole proton following the click reactions is observable in the ^1H NMR spectra most likely due to signal overlap with chemical shifts corresponding to pendant methyl group and pendant aromatic protons, respectively.

Three different samples of PPMC-2 of varying MW were used for subsequent “click” coupling with azide-terminated PS and PEG. The lower MW (R)-PPMC₄₄ (subscript numbers correspond to number of repeat units calculated by ^1H NMR) was coupled with azide-terminated PS₅₇, synthesized via atom transfer radical polymerization (ATRP) according to literature procedures,⁵⁰ to afford (R)-PPMC₄₄-*b*-PS₅₇ (RCP-1). The “click” coupling was successful as demonstrated by GPC showing a single, higher MW distribution corresponding to $M_n = 13.1\text{ kDa}$ and $D = 2.43$ following the reaction (Figure S24).

Two other samples of PPMC-2, denoted (S)-PPMC₁₄₆ and (R)-PPMC₂₀₂, were used for “click” coupling with PEG-azide-1 and -2. The (R)-PPMC₂₀₂ was coupled with commercially available PEG₂₂₅ and PEG₄₅₅ monoazides (PEG-azide-1) forming the diblock, amphiphilic RCPs (R)-PPMC₂₀₂-*b*-PEG₂₂₅ (RCP-2) and (R)-PPMC₂₀₂-*b*-PEG₄₅₅ (RCP-3) with varying hydrophilicity. The GPC of the material following both “click” reactions shows a single MW distribution and a decrease in retention time, confirming the successful coupling of both blocks. The calculated M_n from GPC increases to 48.3 and 53.8 kDa upon click reaction with PEG₂₂₅ and PEG₄₅₅, respectively (Figures S26 and S27). The “click” reaction of (S)-PPMC₁₄₆ with PEG₄₅₅ bisazide (PEG-azide-2) was also confirmed by GPC forming (S)-PPMC₁₄₆-*b*-PEG₄₅₅-*b*-(S)-PPMC₁₄₆ (RCP-4) tri-

block RCP with an increase in M_n to 65.4 kDa (Figure S29), corresponding closely to the attachment of two PPMC chains to the single PEG-azide-2.

Additionally, in most cases, the D values decrease upon “click” reaction due to the decrease in the relative amount of polycarbodiimide, resulting in the decreased adhesion to the stationary phase. For all scans of GPC chromatograms used for MW determination, see the Supporting Information. The tabulated MW data for all homopolymers and copolymers are summarized in Table 1. All other characterization including ^1H NMR, ^{13}C NMR, and IR data can also be found in the Supporting Information.

Table 1. Summarized MW Data for PPMC-2 and Resulting Copolymers Synthesized via Successful Alkyne–Azide “Click” Coupling of End Groups

polymer	n^a	m^a	M_n^a (kDa)	M_n^b (kDa)	D^c	f_{rod}^d
PPMC ₄₄	44		7.0	6.3	2.43	1.0
RCP-1	44	57	11.9	13.1	2.46	0.44
PPMC ₂₀₂	202		32.3	36.3	2.01	1.0
RCP-2	202	225	42.3	48.3	1.77	0.47
RCP-3	202	455	52.3	53.8	1.70	0.31
PPMC ₁₄₆	146		23.4	27.8	2.70	1.0
RCP-4	146	455	66.8	65.4	1.37	0.39

^aCalculated using relative integration of *o*-methyl substituent on aryl end group to the methine pendant group hydrogen. PS and PEG homopolymer MW were also calculated via ^1H NMR end group analysis using the terminal methyl end group and methylene adjacent to the azide, respectively. Block Copolymers M_n were determined from calculated M_n of PPMC-2 added with the M_n of each PEG block and the relative ratios were confirmed by ^1H NMR. ^bCalculated via GPC. ^cDispersity index. ^dMole fraction of polycarbodiimide block calculated from ^1H NMR.

Thermal Characteristics of RCPs. All RCPs shows distinct thermal characteristics associated with each block. Thermogravimetric analysis (TGA) of RCP-1 displays two-step degradation with the first onset of mass loss observed at $T_{d1} = 174^\circ\text{C}$ corresponding to the decomposition of the PPMC block. The second onset of mass loss corresponding to the decomposition of the PS segments occurs at $T_{d2} = 391^\circ\text{C}$ (Figure S10). All three PPMC–PEG block copolymers displayed the same two-step degradation behavior, with the first onset of mass loss corresponding to the PPMC decomposition at $T_{d1} = 174^\circ\text{C}$ and the second mass loss at $T_{d2} = 379^\circ\text{C}$ correlating with the decomposition of PEG (see Supporting Information).

Coupling of the PPMC block to PS-azide was found to slightly reduce the typical glass transition temperature (T_g) observed for PS with $T_g = 81$ and 91°C for RCP-1 and PS-azide, respectively (Figure S11). The intensity of the T_g also is substantially diminished in the copolymer due to the lower relative amount of PS in the system. No thermal transitions are typically observed via DSC for PPMC despite the semicrystalline nature of the helical polymer. This is most likely due to the low degradation temperature of the polymer which occurs below that of any melting transition.

Though PPMC characteristically shows no thermal transitions, the semicrystalline nature of PEG typically displays specific melting endotherms and crystallization exotherms by DSC. The same is true for RCP-2, -3, and -4 with all three showing strong melting transitions upon heating to 60 – 62°C and strong crystallization exotherms at 34 – 36°C upon cooling

(Figure 2). The mass normalized energies associated with the melting transitions are largely identical for all copolymers with values of 83.5 , 84.0 , and 83.6 J/g for RCP-2, -3, and -4, respectively. These thermal transitions will be important to consider when discussing the thin-film morphologies of PPMC–PEG copolymers.

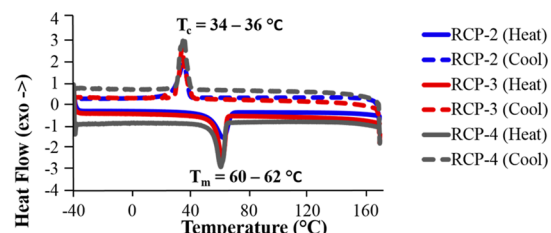


Figure 2. DSC thermogram of RCP-2, -3, and -4 showing strong thermal transitions corresponding to the melting (heat; solid line) and crystallization (cool; dotted line) of the PEG block.

Thin-Film Morphologies of RCPs by AFM. As previously discussed, incorporating rigid-rod, mesogenic blocks with conventional random-coil blocks often leads to interesting morphologies and aggregation behaviors. Grafting PPMC from poly(4-bromostyrene) resulted in the formation of long nanofibular aggregates induced by the mesogenic, self-association behavior of PPMC chains.⁴⁰ The thin-film morphologies of all four RCPs were studied using AFM. The three diblock RCPs (RCP-1–3) displayed similar nanofibular morphologies as shown in the height AFM micrographs in Figure 3.

Both spin-coating and the use of the very flat silicon wafers are imperative in the collection of nicely resolved images for all thin-films studied due to the necessity of uniformity in the surface. Additionally, the added uniformity of spin-coating provides nearly identical thin-film characteristics throughout the entire surface. The nanofibular morphology for RCP-1 was observed when spin-coated from CHCl_3 solutions ($c = 5.0\text{ mg/mL}$) and annealed in CHCl_3 vapor overnight (Figure 3a). The phase AFM image showed largely one phase throughout, suggesting that the PS and PPMC have similar physical and mechanical properties (Figure S30).

The thin films of RCP-2 and -3 spin-coated from CHCl_3 and THF ($c = 5.0\text{ mg/mL}$) without annealing or with only solvent annealing displayed very little order in the height and phase AFM micrographs (see Supporting Information), prompting the need for thermal annealing. The THF cast films were then annealed at 65°C (right above the observed melting temperature for all block copolymers) for 12 h to allow for the films to order and reach their thermodynamically favored morphologies in the melt. This induced the formation of the ordered nanofibular morphologies (Figure 3b,c) with varying phase separated domain sizes as observed by AFM.

The domains of the chemically distinct blocks can be differentiated by the different colors in the AFM phase image (Figure 4). These different colors correspond to the specific response from the AFM cantilever depending on the structural and mechanical properties of the material. Comparing the image for RCP-2 and -3, we observe a large increase in the light-yellow phase that is believed to be a consequence of the increase in MW of the PEG block. For this reason, the yellow phase can be assigned to the hydrophilic PEG block and the dark-brown phase to the PPMC block.

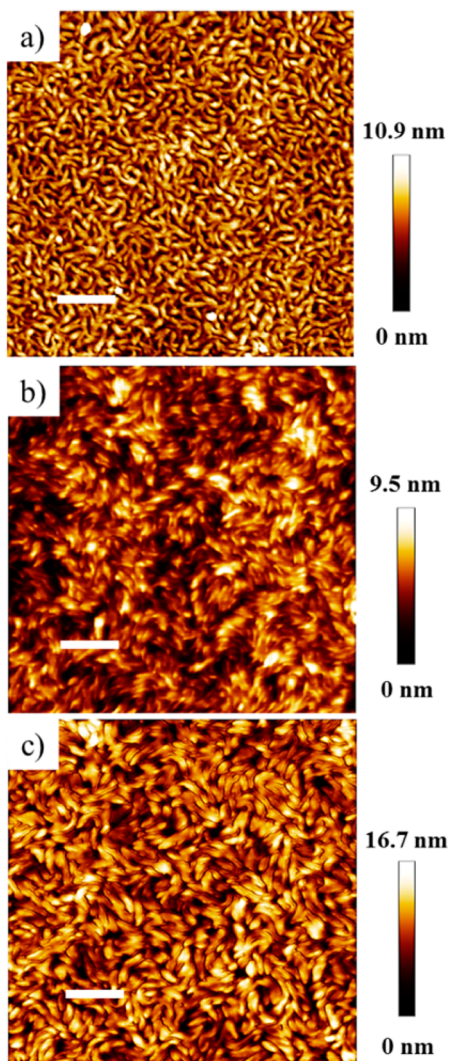


Figure 3. Height AFM micrographs (scan size = $3 \times 3 \mu\text{m}$) of RCP-1 (a), -2 (b), and -3 (c) thin films prepared via different procedures (white scale bar = 500 nm).

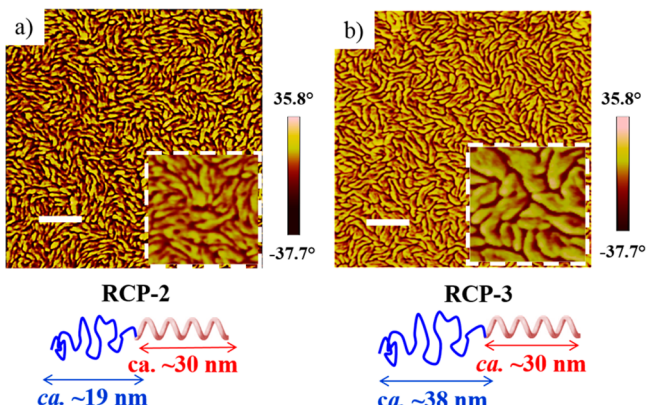


Figure 4. Phase AFM micrograph of RCP-2 (a) and -3 (b) (scan size = $3 \times 3 \mu\text{m}$; inset size = $500 \times 500 \text{ nm}$; white scale bar = 500 nm) displaying distinct phase-separated domains corresponding to the PEG block (yellow) and PPMC block (brown). Also shown are the cartoon representation of the RCPs with the estimated end-to-end distance of each block.

To compare the relative dimensions of each phase-separated domain in the AFM micrographs of RCP-2 and -3, we must first estimate the approximate chain lengths for each block. For the rigid PPMC block with 202 repeating units, the extended chain length is calculated to be 30 nm using the experimentally determined mass-per-length (M_L) value calculated using various light scattering experiments by Nieh et al.⁴¹ This is a good estimate for the MW range of this particular sample due to lack of conformational degrees of freedom resulting in large persistence lengths observed for PPMC.

For the high-MW random-coil PEG chains, however, massive amounts of potential conformations in solution and the solid state are possible due to rotation about the sp^3 -hybridized backbone. This makes the determination of the overall chain length somewhat more difficult and depends heavily on the solvent, temperature, MW, etc. In good solvents for PEG such as THF, the unperturbed root-mean-squared average end-to-end distance ($\langle r^2 \rangle^{1/2}$) can be estimated as a function of MW and viscosity using the Flory–Fox relationship as explained by Dinc et al.⁵¹ Using the calculated values in this article, we estimate the unperturbed chain length of PEG₂₂₅ and PEG₄₅₅ to be 19 and 38 nm, respectively (Figure 4c). Though this calculation is typically used to approximate the dimensions of polymer chains in solution, it provides a decent estimation of the chain length for PEG for the purposes of comparison to AFM images.

AFM allows for the accurate measurements of nanometer-sized features like those observed for RCP-2 and -3. Using the step function in the AFM software, one can easily differentiate the start and end of each phase-separated domain. The average diameter of the dark-brown PPMC phase was measured experimentally for RCP-2 and -3 to be $d_1 = 24 \pm 5$ and 24 ± 4 nm, respectively, matching closely with the calculated extended end-to-end distance of PPMC₂₀₂. Additionally, the identical average diameter is expected since the same sample of PPMC was used in the synthesis of both block copolymers.

The yellow PEG phase, however, nearly doubled in diameter when comparing the AFM of RCP-2 and -3 (ca. $d_2 = 35 \pm 9$ and 61 ± 15 nm, respectively) as expected due to the doubling of MW of the respective PEG chains. Interestingly, the average diameters are significantly larger than the calculated $\langle r^2 \rangle^{1/2}$ values for the PEG chains. In addition, the standard deviation values for the PEG phase diameter are also larger when compared to the PPMC phase. This is believed to be due to the presence of both monolayers (lower bound diameter) and bilayers (upper bound diameter) of the PEG chains throughout the thin film. To confirm or refute the morphological analysis of these copolymers, a series of X-ray scattering experiments will be conducted to unambiguously determine the crystal phase system present throughout the thin film.

The thin-film morphology of the triblock RCP-4 was vastly different than RCP-1, -2, and -3 with well-ordered macroporosity observed throughout the entire surface by AFM. Again, this film was prepared via spin-coating THF solution ($c = 5.0 \text{ mg/mL}$) onto silicon wafers and annealing at 65°C for 12 h. Without thermal annealing, the same craterlike morphology was not observed, and somewhat peculiar phase segregation behaviors were visualized (Figure 5). The unannealed RCP-4 surface was very rough ($\text{RMS}_{\text{roughness}} = 28.0 \text{ nm}$) with large hills observed throughout the continuous thin film in Figure 5a. The AFM phase image (Figure 5c) interestingly displayed circular domains with different phase responses observed toward the center of the hills observed in the height image. Upon thermal annealing, large craters with an average diameter of ca. $832 \pm 194 \text{ nm}$ and depth

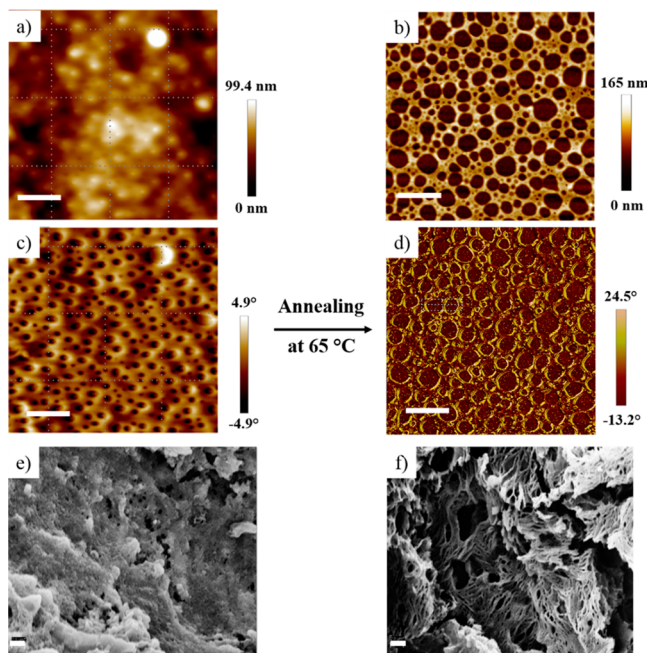


Figure 5. Height (a, b) and phase (c, d) AFM micrograph (a,c: scan size = $5.0 \times 5.0 \mu\text{m}$, scale bar = $1.0 \mu\text{m}$; b,d: scan size = $10 \times 10 \mu\text{m}$, white scale bars = $2.0 \mu\text{m}$) of RCP-4 spin-coated from THF solution ($c = 5.0 \text{ mg/mL}$) before (a, c) and after (b, d) annealing at 65°C displaying the macroporous morphology. Also shown is the SEM micrographs (10000 \times magnification) of bulk polymer precipitated in hexanes from THF solutions before (e) and after (f) annealing at 65°C .

of $82 \pm 6 \text{ nm}$ developed in place of the with largely the same phase throughout the film (Figure 5).

The development of these large craters suggests that there is a large amount of free volume built into the polymer film upon spin-coating from THF. This is hypothesized to be the origin of the observed phase changes when scanning the unannealed polymer film via AFM displaying the dark-brown phase in response to small pockets of free volume. The formation of these pockets will be discussed further in the following section.

The diameters of the craters developed from annealing at 65°C are much larger than the dimensions of each block (ca. 22 nm for each PPEMC₁₄₆ block and again 38 nm for the unperturbed $\langle r^2 \rangle^{1/2}$ value of PEG₄₅₅) so simple phase separation can be ruled out as the real cause of this morphology. To see if this porosity persists in SEM, the copolymer was dissolved in THF, precipitated into hexanes, dried under vacuum, and imaged before and after annealing at 65°C to mimic the sample preparation of the thin-films for AFM (Figure 5e,f). The SEM micrograph of the bulk, annealed material also displayed similar macroporosity in regions of the bulk sample (shown in Figure 5f), further corroborating the morphology viewed in AFM. The SEM of RCP-2 and -3 subject to the same preparation procedure showed no porosity (see Supporting Information), suggesting that this property is specific to RCP-4.

Furthermore, to verify whether these morphologies are indeed evidence of block copolymer formation, a 50:50 wt % blend of PPMC₁₄₆ and PEG₄₅₅ homopolymers was spin-coated from THF (final $c = 5.0 \text{ mg/mL}$) and annealed at 65°C to mimic the thin-film preparation of RCP-2–4. This film, like the RCPs, was imaged via AFM revealing completely different phase separation behaviors. The surface appeared to be composed of a single phase due to the higher surface energy polymer surface migrating during the annealing process (Figure S33).

For all copolymers, the contact angles (CA) of water droplets were measured on thin films prepared following the same protocol used for AFM samples to further analyze the surface composition of the RCPs (Table 2). Reported are both the advancing (θ_{adv}) and receding contact angle (θ_{rec}) to accurately reflect the surface composition.

Table 2. Advancing and Receding Water Contact Angles on Homopolymer and RCP Films Prepared via the Same Protocol Used for AFM Sample Preparation

polymer	advancing CA (θ_{adv} , deg)	receding CA (θ_{rec} , deg)
PPMC ^a	98.9 ± 0.3	67.3 ± 1.2
PS ^a	100.5 ± 0.2	80.9 ± 2.9
RCP-1 ^a	100.9 ± 0.5	80.5 ± 1.0
PEG ^b	77.0 ± 1.0	40.7 ± 2.2
RCP-2 ^b	96.3 ± 0.8	62.1 ± 1.3
RCP-3 ^b	98.9 ± 1.4	62.8 ± 1.4
RCP-4 ^b	34.7 ± 0.8	N/A ^c

^aSpin-coated from CHCl₃ and annealed in CHCl₃ vapor. ^bSpin-coated from THF and annealed at 65°C . ^cDid not recede due to the irreversible wetting of the water drop on the surface.

RCP-1 displayed the highest water CA and lowest hysteresis, as expected, due to the hydrophobic nature of both PPMC and PS. RCP-2 and -3, when spin-coated from THF and annealed at 65°C , have very similar water contact angles (both advancing and receding) which is somewhat surprising due to the increase in PEG content for RCP-3. This is believed to be due to the tightly packed nanofibular morphology in both cases deterring significant surface reorganization. Interestingly, RCP-4 showed much smaller advancing contact angles (ca. $\theta_{\text{adv}} = 34.7^\circ$) and the droplet irreversibly wetted the film. This result suggests that the surface composition of the RCP-4 in and around the large craters consists of mainly PEG which will be considered in the following section.

Aggregation Behavior of RCP-4 in THF. The formation of the submicron size craters observed in AFM and SEM images of RCP-4 is believed to be associated with specific aggregation behaviors of the copolymer in THF solutions. To confirm or refute this hypothesis, AFM was performed on thin RCP-4 films spin-coated from THF at various concentrations ($c = 0.5\text{--}5.0 \text{ mg/mL}$) without any thermal annealing to better understand the mechanism of thin-film formation (Figure 6). This analysis revealed spherical aggregates that, upon increasing concentration, pack tightly together to form the rough thin films observed.

Interestingly, it appears as if the large hills formed by the hypothesized self-association of spherical aggregates increase in diameter as the concentration of the casting solution increases. When cast from the most dilute solution studied ($c = 0.5 \text{ mg/mL}$), the polymeric aggregates cannot fully form a thin film with several large voids observed throughout the sample. Increasing the concentration of the spin-coated solution resulted in a distinct increase in diameter of the observed aggregates and allowed for the thin-film formation composed of these polymeric nanostructures packing together. Spin-coating from $c = 5.0 \text{ mg/mL}$ solutions, in particular, appeared to allow for the ordered formation polymeric nanoparticle arrays with these large aggregates packing closely together forming a continuous, mountainous thin film throughout the sample.

This aggregation behavior was first noticed in the polarizing optical microscope (POM) images of RCP-4 in concentrated

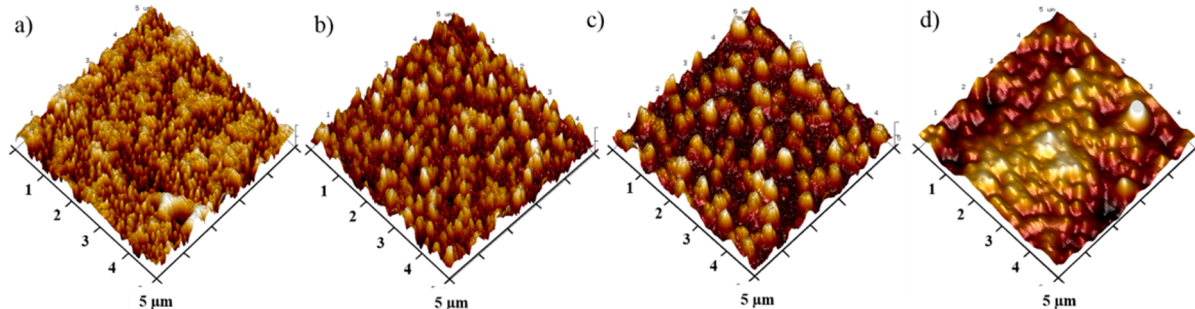


Figure 6. 3D height AFM micrographs (scan size = $5.0 \times 5.0 \mu\text{m}$) of RCP-4 spin-coated from THF solutions of varying concentrations ($c = 0.5$ (a), 1.0 (b), 2.0 (c), and 5.0 mg/mL (d)), revealing the hierarchical self-assembly of spherical polymeric aggregates into a continuous thin film.

THF solutions (ca. 30 and 40 wt %) where we observed large spherical aggregates believed to be microcapsule/polymersome assemblies (Figure 7). These same aggregates were not observed for RCP-2 and -3 in concentrated THF solutions as evidenced by the black POM image, suggesting the solution is completely isotropic.

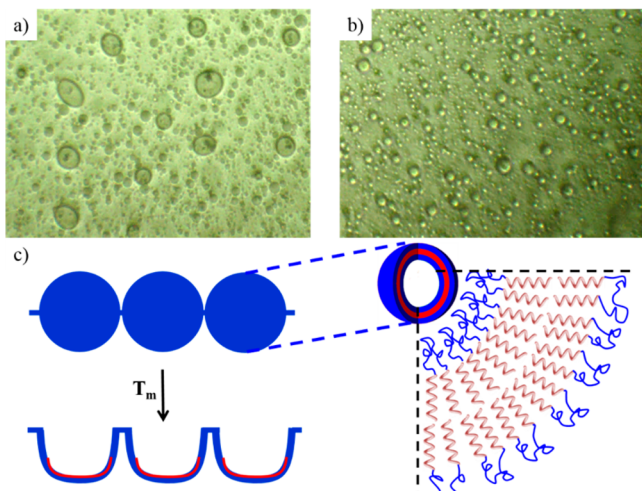


Figure 7. POM images of RCP-4 in concentrated 30 wt % (a) and 40 wt % (b) THF solutions showing the large polymersome microcapsule aggregates (160 \times magnification). Also depicted is the hypothesized ordering of the microcapsules upon solvent evaporation and melting of the aggregates forming the large, submicron diameter craters observed in AFM (c).

Upon solvent evaporation, we propose that these vesicle-like aggregates order themselves into a thin film and are frozen into place when all the solvent is removed. The large diameters of these aggregates suggest that they may possess a hollow interior which would explain the hypothesized free-volume associated with the thin film. Increasing the temperature to 65 °C, above the observed T_m of RCP-4, causes the surrounding walls of the polymersome (consisting of the copolymer ordered with the PPMC chains on the interior of the bilayer; see Figure 7c) melted, filling the free volume of the hollow interior, forming the submicron diameter craters observed in the AFM. A similar mechanism was described by Pietsch et al. in recent work detailing the ordering of metal-loaded block copolymer vesicles into thin films followed by chemical etching to form nano- and microporous honeycomb morphologies.⁵² This hypothesis would also explain the smaller water contact angles on RCP-4 films due to the PEG blocks being exclusively exposed on the

surface. Additionally, the large craters can essentially act as hydrophilic wells for the water to occupy causing the irreversible wetting that was noted previously.

To observe if these aggregates persist in more dilute solutions, like those used for AFM sample preparation, we employed dynamic light scattering (DLS) to measure the size RCP-4 aggregates in THF solutions at various concentrations. Interestingly, the polymersome diameters were found to increase in a linear fashion as the concentration of the polymer solution increases (Figure 8). At each concentration, we observed a single, narrow size distribution associated with the spherical polymersome aggregates.

In dilute 5.0 mg/mL THF solutions, the Z-average hydrodynamic diameter (D_h) of the RCP-4 aggregates was found to be ca. 272.0 nm by DLS cumulant analysis. Increasing the concentration greatly affected the size of the polymeric

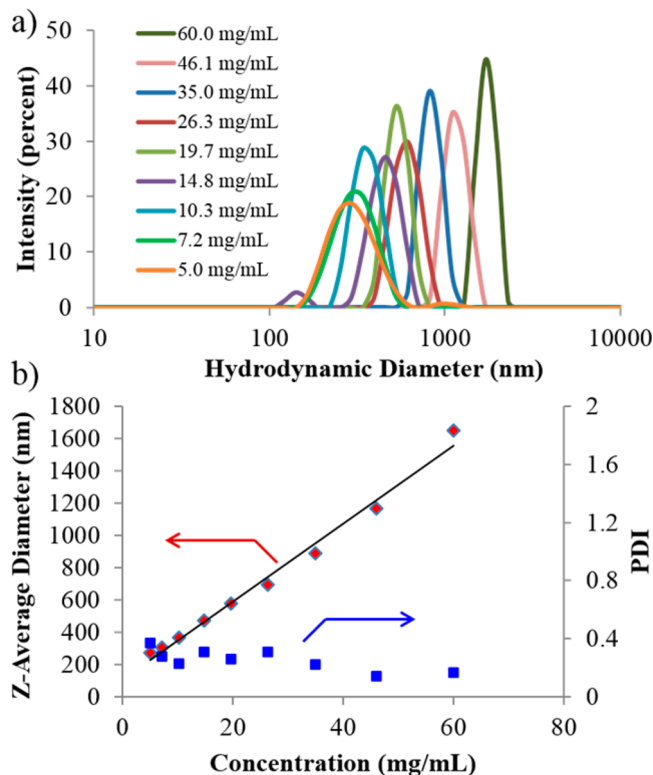


Figure 8. DLS plots of hydrodynamic diameter (D_h) vs intensity (a) and Z-average diameter/PDI vs concentration (b) for RCP-4 THF solutions showing a linear dependence of polymersome diameter as a function of concentration.

nanoparticles in solution with distinct increases of Z-average D_h values up to ca. 1648 nm at $c = 60.0$ mg/mL. At concentrations lower than 5.0 mg/mL and greater than 60 mg/mL, the aggregate size plateaus suggesting that this is the full range of polymersome size in THF solutions. Interestingly, the PDI values provided by DLS, not to be confused with D discussed earlier, seemed to decrease, with a few exceptions, as the concentration and D_h increase. The PDI values range from 0.369 at low concentrations, like 5.0 mg/mL, to 0.166 at high concentrations, like 60 mg/mL. The latter is surprisingly monodisperse since PDIs < 0.2 are very rare for dynamic nanoparticles in solution.⁵³ The self-assembly and aggregation behavior of all amphiphilic PPMC–PEG copolymers (**RCP-2–4**) in selective solvents for PEG such as H₂O and MeOH will be discussed in detail in a follow-up paper.

Lyotropic Liquid Crystallinity of RCPs. As mentioned earlier, PPMC chains adopt well-ordered lyotropic cholesteric mesophases in concentrated CHCl₃ solutions (ca. 12.5 wt %).³⁵ To test if this property persists, the four copolymers were dissolved in concentrated CHCl₃, toluene, and THF solutions with a range of concentrations from 15 to 40 wt % to screen their liquid crystallinity. **RCP-1** displayed no liquid crystalline (LC) behaviors in all solvents most likely due to the amorphous nature of the PS blocks preventing significant ordering in solution. **RCP-2**, -3, and -4, however, displayed ordered cholesteric mesophases in 30 wt % toluene solutions as observed by POM (Figure 9). All three copolymers displayed the same spherulite,

polygonal texture typical of cholesteric mesophases. Interestingly, all copolymers displayed no LC order in CHCl₃ solutions despite the order observed for PPMC homopolymers. This is believed to be due to the good solubility of the random-coil blocks in CHCl₃ disrupting the ordered packing of the anisotropic PPMC blocks. In toluene, however, the PEG blocks most likely adopt a collapsed structure due to their poor solubility, which allows for the added ordering of the PPMC chains. Another driving force for the anisotropy observed via POM for **RCP-2–4** could be crystallization of the PEG blocks into the spherulitic birefringence visualized in Figure 9. These spherulites are intermixed, in all cases, with the clear cholesteric birefringence resulting from the helical ordering of the chiral PPMC chains. Additional experiments, including X-ray scattering methods, are necessary to fully understand the level of ordering in such liquid crystals and will be conducted in future work.

CONCLUSIONS

The alkyne end-functionalized **PPMC-2**, synthesized using the protected alkyne functional nickel(II) initiator **Ni-1** followed by deprotection with TBAF, was successfully coupled with azide-terminated PS and PEG via CuAAC “click” reaction forming a novel class of helical-*b*-random coil RCPs. In the thin film, the three diblock copolymers (**RCP-1–3**) adopted interesting nanofibular morphologies as observed by AFM. The PPMC–PEG diblock copolymers **RCP-2** and -3 displayed distinct phase separation which allowed for the quantitative measurements of each specific domain associated with each block by AFM. The measured dimensions of each domain match closely with the calculated unperturbed end-to-end distance of each block, providing further evidence for the proposed morphology.

RCP-4, however, adopted unique macroporous morphologies with an average pore size of ca. 832 ± 194 nm observed by both AFM and SEM when cast from THF and annealed at 65 °C for 12 h. The formation of this morphology is hypothesized to be attributed to the ordering of large, polymersome aggregates, identified by POM, into the thin-film upon solvent evaporation. The thermal annealing at 65 °C, above the T_m of **RCP-4**, then melts the polymersome walls filling the hollow interior, creating the submicron craters observed.

Furthermore, the self-assembly behavior of **RCP-4** in THF was studied by DLS showing a strong relationship between vesicle diameter and concentration. Altering the concentration of the THF solutions from $c = 5.0$ mg/mL to $c = 60.0$ mg/mL caused a linear increase in polymersome diameter from ca. 272.0 to 1648 nm as evidenced by DLS. Finally, the PPMC–PEG block copolymers were found to adopt lyotropic cholesteric LC mesophases in concentrated toluene solutions. This method marks one of the simplest and most versatile approaches to forming RCPs with fully synthetic helical, rigid-rod segments of varying MW. These novel materials have proven to possess a variety of interesting and fruitful properties opening up the possibility for several potential applications such as drug delivery, biological mimics, and tunable nanoscale morphological design.

ASSOCIATED CONTENT

S Supporting Information

Additional characterization data for all copolymers. The Supporting Information is available free of charge on the ACS Publications website at DOI: 10.1021/acs.macromol.5b00453.

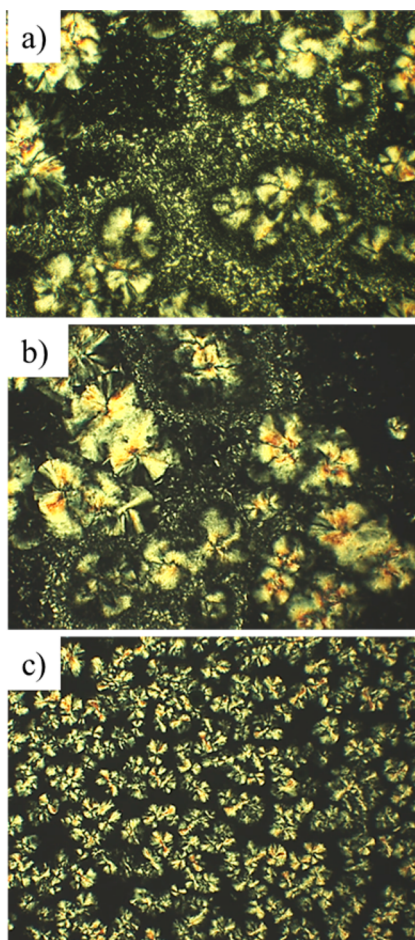


Figure 9. POM images (40× magnification) of **RCP-2** (a), -3 (b), and -4 (c) in concentrated (30 wt %) toluene solutions displaying ordered, lyotropic cholesteric LC mesophases.

AUTHOR INFORMATION

Corresponding Author

*E-mail: bxn111230@utdallas.edu (B.M.N.).

Notes

The authors declare no competing financial interest.

ACKNOWLEDGMENTS

Funding for this work was provided by the Faculty start-up fund from the University of Texas at Dallas (UTD) and the Endowed Chair for Excellence at UTD. We gratefully acknowledge the NSF-MRI grant (CHE-1126177) used to purchase the Bruker AVANCE III 500 NMR instrument.

REFERENCES

- (1) Bates, F. S.; Fredrickson, G. H. *Phys. Today* **1999**, *52* (2), 32–38.
- (2) Stupp, S. I.; LeBonheur, V.; Walker, K.; Li, L. S.; Huggins, K. E.; Keser, M.; Amstutz, A. *Science* **1997**, *276* (5311), 384–389.
- (3) Klok, H.-A.; Lecommandoux, S. *Adv. Mater.* **2001**, *13* (16), 1217–1229.
- (4) Lee, M.; Cho, B.-K.; Zin, W.-C. *Chem. Rev.* **2001**, *101* (12), 3869–3892.
- (5) Lee, M.; Yoo, Y.-S. *J. Mater. Chem.* **2002**, *12* (8), 2161–2168.
- (6) Zhang, J.; Chen, X.-F.; Wei, H.-B.; Wan, X.-H. *Chem. Soc. Rev.* **2013**, *42* (23), 9127–9154.
- (7) Floudas, G.; Papadopoulos, P.; Klok, H. A.; Vandermeulen, G. W. M.; Rodriguez-Hernandez, J. *Macromolecules* **2003**, *36* (10), 3673–3683.
- (8) Wu, J.; Pearce, E. M.; Kwei, T. K. *Macromolecules* **2001**, *34* (6), 1828–1836.
- (9) Kim, B.-S.; Hong, D.-J.; Bae, J.; Lee, M. *J. Am. Chem. Soc.* **2005**, *127* (46), 16333–16337.
- (10) Wang, H.; Wang, H. H.; Urban, V. S.; Littrell, K. C.; Thiagarajan, P.; Yu, L. *J. Am. Chem. Soc.* **2000**, *122* (29), 6855–6861.
- (11) Koenig, H. M.; Gorelik, T.; Kolb, U.; Kilbinger, A. F. M. *J. Am. Chem. Soc.* **2007**, *129* (3), 704–708.
- (12) Schleuss, T. W.; Abbel, R.; Gross, M.; Schollmeyer, D.; Frey, H.; Maskos, M.; Berger, R.; Kilbinger, A. F. M. *Angew. Chem., Int. Ed.* **2006**, *45* (18), 2969–2975.
- (13) Chiu, Y.-C.; Chen, Y.; Kuo, C.-C.; Tung, S.-H.; Kakuchi, T.; Chen, W.-C. *ACS Appl. Mater. Interfaces* **2012**, *4* (7), 3387–3395.
- (14) Lu, S.; Liu, T.; Ke, L.; Ma, D.-G.; Chua, S.-J.; Huang, W. *Macromolecules* **2005**, *38* (20), 8494–8502.
- (15) Kamps, A. C.; Fryd, M.; Park, S.-J. *ACS Nano* **2012**, *6* (3), 2844–2852.
- (16) Iovu, M. C.; Craley, C. R.; Jeffries-El, M.; Krankowski, A. B.; Zhang, R.; Kowalewski, T.; McCullough, R. D. *Macromolecules* **2007**, *40* (14), 4733–4735.
- (17) Chen, X. L.; Jenekhe, S. A. *Macromolecules* **2000**, *33* (13), 4610–4612.
- (18) Jenekhe, S. A.; Chen, X. L. *Science* **1998**, *279* (5358), 1903–1907.
- (19) Jenekhe, S. A.; Chen, X. L. *Science* **1999**, *283* (5400), 372–375.
- (20) Cai, C.; Li, Y.; Lin, J.; Wang, L.; Lin, S.; Wang, X.-S.; Jiang, T. *Angew. Chem., Int. Ed.* **2013**, *52* (30), 7732–7736.
- (21) Cai, C.; Lin, J.; Chen, T.; Wang, X.-S.; Lin, S. *Chem. Commun.* **2009**, *19*, 2709–2711.
- (22) Ibarboure, E.; Papon, E.; Rodriguez-Hernandez, J. *Polymer* **2007**, *48* (13), 3717–3725.
- (23) Ibarboure, E.; Rodriguez-Hernandez, J. *Eur. Polym. J.* **2010**, *46* (5), 891–899.
- (24) Yang, Z.; Yuan, J.; Cheng, S. *Eur. Polym. J.* **2005**, *41* (2), 267–274.
- (25) Huang, C.-J.; Chang, F.-C. *Macromolecules* **2008**, *41* (19), 7041–7052.
- (26) Rao, J.; Luo, Z.; Ge, Z.; Liu, H.; Liu, S. *Biomacromolecules* **2007**, *8* (12), 3871–3878.
- (27) Loos, K.; Boeker, A.; Zettl, H.; Zhang, M.; Krausch, G.; Mueller, A. H. E. *Macromolecules* **2005**, *38* (3), 873–879.
- (28) Chen, J. T.; Thomas, E. L.; Ober, C. K.; Hwang, S. S. *Macromolecules* **1995**, *28* (5), 1688–97.
- (29) Liu, X.; Deng, J.; Wu, Y.; Zhang, L. *Polymer* **2012**, *53* (25), 5717–5722.
- (30) Rahman, M. S.; Changez, M.; Yoo, J.-W.; Lee, C. H.; Samal, S.; Lee, J.-S. *Macromolecules* **2008**, *41* (19), 7029–7032.
- (31) Wu, J.; Pearce, E. M.; Kwei, T. K.; Lefebvre, A. A.; Balsara, N. P. *Macromolecules* **2002**, *35* (5), 1791–1796.
- (32) Satoh, T.; Ihara, R.; Kawato, D.; Nishikawa, N.; Suemasa, D.; Kondo, Y.; Fuchise, K.; Sakai, R.; Kakuchi, T. *Macromolecules* **2012**, *45* (9), 3677–3686.
- (33) Goodwin, A.; Novak, B. M. *Macromolecules* **1994**, *27*, 5520–2.
- (34) Kim, J.; Novak, B. M.; Waddon, A. J. *Macromolecules* **2004**, *37*, 1660–1662.
- (35) Kim, J.; Novak, B. M.; Waddon, A. J. *Macromolecules* **2004**, *37*, 8286–8292.
- (36) Schlitzer, D. S.; Novak, B. M. *J. Am. Chem. Soc.* **1998**, *120*, 2196–2197.
- (37) Kennemur, J. G.; Clark, J. B.; Tian, G.; Novak, B. M. *Macromolecules* **2010**, *43*, 1867–1873.
- (38) Merten, C.; Reuther, J. F.; De Sousa, J. D.; Novak, B. M. *Phys. Chem. Chem. Phys.* **2014**, *16* (23), 11456–11460.
- (39) Reuther, J. F.; Novak, B. M. *J. Am. Chem. Soc.* **2013**, *135* (51), 19292–19303.
- (40) Reuther, J. F.; Bhatt, M. P.; Tian, G.; Batchelor, B. L.; Campos, R.; Novak, B. M. *Macromolecules* **2014**, *47* (14), 4587–4595.
- (41) Nieh, M.-P.; Goodwin, A. A.; Stewart, J. R.; Novak, B. M.; Hoagland, D. A. *Macromolecules* **1998**, *31*, 3151–3154.
- (42) Pang, X.-C.; Zhao, L.; Feng, C.-W.; Lin, Z.-Q. *Macromolecules* **2011**, *44* (18), 7176–7183.
- (43) Pang, X.; Zhao, L.; Feng, C.; Wu, R.; Ma, H.; Lin, Z. *Polym. Chem.* **2013**, *4* (6), 2025–2032.
- (44) Pang, X.; Feng, C.; Xu, H.; Han, W.; Xin, X.; Xia, H.; Qiu, F.; Lin, Z. *Polym. Chem.* **2014**, *5* (8), 2747–2755.
- (45) Feng, C.; Pang, X.; He, Y.; Li, B.; Lin, Z. *Chem. Mater.* **2014**, *26* (20), 6058–6067.
- (46) Budhathoki-Uprety, J.; Novak, B. M. *Macromolecules* **2011**, *44* (15), 5947–5954.
- (47) Budhathoki-Uprety, J.; Peng, L. L.; Melander, C.; Novak, B. M. *ACS Macro Lett.* **2012**, *1* (3), 370–374.
- (48) Budhathoki-Uprety, J.; Reuther, J. F.; Novak, B. M. *Macromolecules* **2012**, *45* (20), 8155–8165.
- (49) Smeets, A.; Van den Bergh, K.; De Winter, J.; Gerbaux, P.; Verbiest, T.; Koeckelberghs, G. *Macromolecules* **2009**, *42* (20), 7638–7641.
- (50) Matyjaszewski, K.; Nakagawa, Y.; Gaynor, S. G. *Macromol. Rapid Commun.* **1997**, *18* (12), 1057–1066.
- (51) Ding, C. Ö.; Kibarer, G.; Güner, A. J. *Appl. Polym. Sci.* **2010**, *117* (2), 1100–1119.
- (52) Pietsch, T.; Gindy, N.; Fahmi, A. *Soft Matter* **2009**, *5* (11), 2188–2197.
- (53) Zhang, S.; Sun, H.-J.; Hughes, A. D.; Draghici, B.; Lejnieks, J.; Leowanawat, P.; Bertin, A.; Otero De Leon, L.; Kulikov, O. V.; Chen, Y.; Pochan, D. J.; Heiney, P. A.; Percec, V. *ACS Nano* **2014**, *8* (2), 1554–1565.